Collagen quantification in breast tissue using a 12-wavelength near infrared spectral tomography (NIRST) system

YAN ZHAO,[1] WILLIAM R. BURGER,[1] MINGWEI ZHOU,[1] ERICA B. BERNHARDT,[2] PETER A. KAUFMAN,[2,3] ROSHANI R. PATEL,[2] CHRISTINA V. ANGELES,[2] BRIAN W. POGUE,[1,2] KEITH D. PAULSEN,[1,2] AND SHUDONG JIANG[1,2,*]

[1]Thayer School of Engineering, Dartmouth College, Hanover, NH 03755, USA
[2]Norris Cotton Cancer Center, Dartmouth-Hitchcock Medical Center, Lebanon NH 03756, USA
[3]Department of Medicine, Geisel School of Medicine, Dartmouth College, Hanover NH 03755, USA
[*]shudong.jiang@dartmouth.edu

Abstract: A portable near infrared spectral tomography (NIRST) system was adapted for breast cancer detection and treatment monitoring with improved speed of acquisition for parallel 12 wavelengths of parallel frequency-domain (FD) and continuous-wavelength (CW) measurement. Using a novel gain adjustment scheme in the Photomultiplier Tube detectors (PMTs), the data acquisition time for simultaneous acquisition involving three FD and three CW wavelengths, has been reduced from 90 to 55 seconds, while signal variation was also reduced from 2.1% to 1.1%. Tomographic images of breast collagen content have been recovered for the first time, and image reconstruction approaches with and without collagen content included have been validated in simulation studies and normal subject exams. Simulations indicate that including collagen content into the reconstruction procedure can significantly reduce the overestimation in total hemoglobin, water and lipid by 8.9μM, 1.8% and 15.8%, respectively, and underestimates in oxygen saturation by 9.5%, given an average 10% background collagen content. A breast cancer patient with invasive ductal carcinoma was imaged and the reconstructed images show that the recovered tumor/background contrast in total hemoglobin increased from 1.5 to 1.7 when collagen was included in reconstruction.

References and links

1. W. J. Gradishar, B. O. Anderson, S. L. Blair, H. J. Burstein, A. Cyr, A. D. Elias, W. B. Farrar, A. Forero, S. H. Giordano, L. J. Goldstein, D. F. Hayes, C. A. Hudis, S. J. Isakoff, B. M. Ljung, P. K. Marcom, I. A. Mayer, B. McCormick, R. S. Miller, M. Pegram, L. J. Pierce, E. C. Reed, K. E. Salerno, L. S. Schwartzberg, M. L. Smith, H. Soliman, G. Somlo, J. H. Ward, A. C. Wolff, R. Zellars, D. A. Shead, and R. Kumar; National Comprehensive Cancer Network Breast Cancer Panel, "Breast cancer version 3.2014," J. Natl. Compr. Canc. Netw. **12**(4), 542–590 (2014).
2. B. Fisher, A. Brown, E. Mamounas, S. Wieand, A. Robidoux, R. G. Margolese, A. B. Cruz, Jr., E. R. Fisher, D. L. Wickerham, N. Wolmark, A. DeCillis, J. L. Hoehn, A. W. Lees, and N. V. Dimitrov, "Effect of preoperative chemotherapy on local-regional disease in women with operable breast cancer: findings from National Surgical Adjuvant Breast and Bowel Project B-18," J. Clin. Oncol. **15**(7), 2483–2493 (1997).
3. I. C. Smith, S. D. Heys, A. W. Hutcheon, I. D. Miller, S. Payne, F. J. Gilbert, A. K. Ah-See, O. Eremin, L. G. Walker, T. K. Sarkar, S. P. Eggleton, and K. N. Ogston, "Neoadjuvant chemotherapy in breast cancer: significantly enhanced response with docetaxel," J. Clin. Oncol. **20**(6), 1456–1466 (2002).
4. A. Cerussi, D. Hsiang, N. Shah, R. Mehta, A. Durkin, J. Butler, and B. J. Tromberg, "Predicting response to breast cancer neoadjuvant chemotherapy using diffuse optical spectroscopy," Proc. Natl. Acad. Sci. U.S.A. **104**(10), 4014–4019 (2007).
5. E. Yeh, P. Slanetz, D. B. Kopans, E. Rafferty, D. Georgian-Smith, L. Moy, E. Halpern, R. Moore, I. Kuter, and A. Taghian, "Prospective comparison of mammography, sonography, and MRI in patients undergoing neoadjuvant chemotherapy for palpable breast cancer," AJR Am. J. Roentgenol. **184**(3), 868–877 (2005).

6. D. A. Mankoff, L. K. Dunnwald, J. R. Gralow, G. K. Ellis, M. J. Drucker, and R. B. Livingston, "Monitoring the response of patients with locally advanced breast carcinoma to neoadjuvant chemotherapy using [technetium 99m]-sestamibi scintimammography," Cancer **85**(11), 2410–2423 (1999).

7. A. Corlu, R. Choe, T. Durduran, M. A. Rosen, M. Schweiger, S. R. Arridge, M. D. Schnall, and A. G. Yodh, "Three-dimensional in vivo fluorescence diffuse optical tomography of breast cancer in humans," Opt. Express **15**(11), 6696–6716 (2007).

8. L. Xi, X. Li, L. Yao, S. Grobmyer, and H. Jiang, "Design and evaluation of a hybrid photoacoustic tomography and diffuse optical tomography system for breast cancer detection," Med. Phys. **39**(5), 2584–2594 (2012).

9. Y. Hoshi and Y. Yamada, "Overview of diffuse optical tomography and its clinical applications," J. Biomed. Opt. **21**(9), 091312 (2016).

10. A. Cerussi, N. Shah, D. Hsiang, A. Durkin, J. Butler, and B. J. Tromberg, "In vivo absorption, scattering, and physiologic properties of 58 malignant breast tumors determined by broadband diffuse optical spectroscopy," J. Biomed. Opt. **11**(4), 044005 (2006).

11. M. L. Flexman, H. K. Kim, J. E. Gunther, E. A. Lim, M. C. Alvarez, E. Desperito, K. Kalinsky, D. L. Hershman, and A. H. Hielscher, "Optical biomarkers for breast cancer derived from dynamic diffuse optical tomography," J. Biomed. Opt. **18**(9), 096012 (2013).

12. H. Y. Ban, M. Schweiger, V. C. Kavuri, J. M. Cochran, L. Xie, D. R. Busch, J. Katrašnik, S. Pathak, S. H. Chung, K. Lee, R. Choe, B. J. Czerniecki, S. R. Arridge, and A. G. Yodh, "Heterodyne frequency-domain multispectral diffuse optical tomography of breast cancer in the parallel-plane transmission geometry," Med. Phys. **43**(7), 4383–4395 (2016).

13. P. Taroni, G. Danesini, A. Torricelli, A. Pifferi, L. Spinelli, and R. Cubeddu, "Clinical trial of time-resolved scanning optical mammography at 4 wavelengths between 683 and 975 nm," J. Biomed. Opt. **9**(3), 464–473 (2004).

14. N. Shah, A. Cerussi, C. Eker, J. Espinoza, J. Butler, J. Fishkin, R. Hornung, and B. Tromberg, "Noninvasive functional optical spectroscopy of human breast tissue," Proc. Natl. Acad. Sci. U.S.A. **98**(8), 4420–4425 (2001).

15. B. W. Pogue, S. P. Poplack, T. O. McBride, W. A. Wells, K. S. Osterman, U. L. Osterberg, and K. D. Paulsen, "Quantitative hemoglobin tomography with diffuse near-infrared spectroscopy: pilot results in the breast," Radiology **218**(1), 261–266 (2001).

16. V. Ntziachristos, A. G. Yodh, M. D. Schnall, and B. Chance, "MRI-guided diffuse optical spectroscopy of malignant and benign breast lesions," Neoplasia **4**(4), 347–354 (2002).

17. B. E. Schaafsma, M. van de Giessen, A. Charehbili, V. T. Smit, J. R. Kroep, B. P. Lelieveldt, G.-J. Liefers, A. Chan, C. W. Löwik, J. Dijkstra, C. J. van de Velde, M. N. Wasser, and A. L. Vahrmeijer, "Optical mammography using diffuse optical spectroscopy for monitoring tumor response to neoadjuvant chemotherapy in women with locally advanced breast cancer," Clin. Cancer Res. **21**(3), 577–584 (2015).

18. Q. Zhu, P. A. DeFusco, A. Ricci, Jr., E. B. Cronin, P. U. Hegde, M. Kane, B. Tavakoli, Y. Xu, J. Hart, and S. H. Tannenbaum, "Breast cancer: assessing response to neoadjuvant chemotherapy by using US-guided near-infrared tomography," Radiology **266**(2), 433–442 (2013).

19. D. Roblyer, S. Ueda, A. Cerussi, W. Tanamai, A. Durkin, R. Mehta, D. Hsiang, J. A. Butler, C. McLaren, W.-P. Chen, and B. Tromberg, "Optical imaging of breast cancer oxyhemoglobin flare correlates with neoadjuvant chemotherapy response one day after starting treatment," Proc. Natl. Acad. Sci. U.S.A. **108**(35), 14626–14631 (2011).

20. S. Jiang, B. W. Pogue, P. A. Kaufman, J. Gui, M. Jermyn, T. E. Frazee, S. P. Poplack, R. DiFlorio-Alexander, W. A. Wells, and K. D. Paulsen, "Predicting breast tumor response to neoadjuvant chemotherapy with Diffuse Optical Spectroscopic Tomography prior to treatment," Clin. Cancer Res. **20**(23), 6006–6015 (2014).

21. C. Xu, H. Vavadi, A. Merkulov, H. Li, M. Erfanzadeh, A. Mostafa, Y. Gong, H. Salehi, S. Tannenbaum, and Q. Zhu, "Ultrasound-guided diffuse optical tomography for predicting and monitoring neoadjuvant chemotherapy of breast cancers: recent progress," Ultrason. Imaging **38**(1), 5–18 (2016).

22. B. J. Tromberg, Z. Zhang, A. Leproux, T. D O'Sullivan, A. E. Cerussi, P. Carpenter, R. S. Mehta, D. Roblyer, W. Yang, and K. D. Paulsen, "Predicting Responses to Neoadjuvant Chemotherapy in Breast Cancer: ACRIN 6691 Trial of Diffuse Optical Spectroscopic Imaging (DOSI)," Cancer Res. **76**, 5933 (2016).

23. P. Taroni, A. M. Paganoni, F. Ieva, A. Pifferi, G. Quarto, F. Abbate, E. Cassano, and R. Cubeddu, "Non-invasive optical estimate of tissue composition to differentiate malignant from benign breast lesions: A pilot study," Sci. Rep. **7**, 40683 (2017).

24. J. Wang, B. W. Pogue, S. Jiang, and K. D. Paulsen, "Near-infrared tomography of breast cancer hemoglobin, water, lipid, and scattering using combined frequency domain and cw measurement," Opt. Lett. **35**(1), 82–84 (2010).

25. Y. Zhao, B. W. Pogue, S. J. Haider, J. Gui, R. M. diFlorio-Alexander, K. D. Paulsen, and S. Jiang, "Portable, parallel 9-wavelength near-infrared spectral tomography (NIRST) system for efficient characterization of breast cancer within the clinical oncology infusion suite," Biomed. Opt. Express **7**(6), 2186–2201 (2016).

26. H. Dehghani, M. E. Eames, P. K. Yalavarthy, S. C. Davis, S. Srinivasan, C. M. Carpenter, B. W. Pogue, and K. D. Paulsen, "Near infrared optical tomography using NIRFAST: Algorithm for numerical model and image reconstruction," Commun. Numer. Methods Eng. **25**(6), 711–732 (2009).

27. Y. Zhao, M. A. Mastanduno, S. Jiang, F. Ei-Ghussein, J. Gui, B. W. Pogue, and K. D. Paulsen, "Optimization of image reconstruction for magnetic resonance imaging-guided near-infrared diffuse optical spectroscopy in breast," J. Biomed. Opt. **20**(5), 056009 (2015).

28. P. Taroni, D. Comelli, A. Pifferi, A. Torricelli, and R. Cubeddu, "Absorption of collagen: effects on the estimate of breast composition and related diagnostic implications," J. Biomed. Opt. **12**, 014021 (2007).
29. J. Jung, R. Istfan, and D. Roblyer, "Note: A simple broad bandwidth undersampling frequency-domain digital diffuse optical spectroscopy system," Rev. Sci. Instrum. **85**(7), 076108 (2014).
30. F. El-Ghussein, M. A. Mastanduno, S. Jiang, B. W. Pogue, and K. D. Paulsen, "Hybrid photomultiplier tube and photodiode parallel detection array for wideband optical spectroscopy of the breast guided by magnetic resonance imaging," J. Biomed. Opt. **19**(1), 011010 (2013).
31. J. Wang, S. Jiang, Z. Li, R. M. diFlorio-Alexander, R. J. Barth, P. A. Kaufman, B. W. Pogue, and K. D. Paulsen, "In vivo quantitative imaging of normal and cancerous breast tissue using broadband diffuse optical tomography," Med. Phys. **37**(7), 3715–3724 (2010).
32. G. Quarto, L. Spinelli, A. Pifferi, A. Torricelli, R. Cubeddu, F. Abbate, N. Balestreri, S. Menna, E. Cassano, and P. Taroni, "Estimate of tissue composition in malignant and benign breast lesions by time-domain optical mammography," Biomed. Opt. Express **5**(10), 3684–3698 (2014).

1. Introduction

Breast cancer is a complex disease that presents challenges for both detection, treatment, and treatment monitoring. The traditional treatment strategy has been surgery, or surgery and radiation therapy, followed by adjuvant chemotherapy [1]. However, neoadjuvant chemotherapy (NAC) prior to surgery is being increasingly utilized [2]. This is especially the case for several molecular subtypes, according to expression of estrogen receptor (ER), progesterone receptor (PR), and human epidermal growth factor 2 (HER2). Ultimately the goal of all of these approaches is prevention of distant metastases, as well as locoregional recurrence [3]. Numerous clinical studies have shown that neoadjuvant tumor response varies between these specific molecular subtypes of breast cancer, specifically being ER/PR + , HER2 + , and triple negative breast cancer, in which none of these receptors are expressed. The current standard of care in determining response to NAC is pathology, and specifically the demonstration of a pathologic complete response. However, several studies are beginning to suggest imaging biomarkers may be accurate, which would be of enormous clinical utility [4]. Multiple imaging modalities including ultrasound, mammography and MRI, have shown success in monitoring tumor response but still have limitations [5, 6]. Compared to these imaging modalities, near infrared spectroscopy (NIRS) and spectral tomography (NIRST) provide potential advantages due to their noninvasive nature, relatively low cost and portable size [7–9]. Pilot studies have shown that NIRS and NIRST can assess the intrinsic biophysical composition of tissue, in terms of absorber concentrations of deoxy-hemoglobin (Hb) and oxy-hemoglobin (HbO), water and lipids [10–12], as well as the scattering signatures attributed to ultra-structural cellular density and size ensemble associated with the extracellular matrix and subcellular constituents in healthy breast tissues [13, 14]. These can differentiate malignant from benign pathology [15, 16], and have shown success in monitoring the tumor response to treatments [17–22]. In addition to total hemoglobin (HbT, sum of oxy- and deoxy-hemoglobin) and oxygen saturation (StO_2, the ratio of oxy-hemoglobin to HbT), recent studies suggested that the extracellular water fraction occurring during the earliest stages of NAC is a biomarker of tumor response to therapy because they accompany apoptotic cell shrinkage [20]. Taroni *et al* has recently shown collagen as one important biomarker in pathologic classification, as concluded from a clinical study using an optical mammography system operating with seven wavelengths (635nm to 1060nm) [23]. However, there are no publications testing the quantification of collagen in breast tissues with tomographic capabilities. While frequency domain (FD) NIRST can estimate water content in the breast as well as oxy- and deoxy-hemoglobin based on the known molar absorption spectra in the near infrared range, the accuracy to assess lipid and collagen content is limited by the sensitivity limitation of its optical detectors (Photomultiplier Tubes) beyond 850nm where pertinent spectral features reside. To address these challenges, a combined FD and continuous wave (CW) approach with enhanced spectral coverage has been shown to improve the separation of water/lipid from Hb and HbO contributions in breast tissue [24].

In this paper, our previous system [25] was modified to combine 12-wavelengths of FD (capturing the complete tissue features in the 660-852nm wavelength range) and CW (for

additional lipid and collagen features shown in the wavelength range of 850-1064nm). This NIRST system has been developed with two sets of simultaneous acquisitions of three FD and three CW wavelengths. A novel gain adjustment approach of the PMTs was been encoded into the system to expedite data acquisition and reduce signal fluctuation. Simulations, normal subjects and breast cancer patient studies have been conducted to validate an image reconstruction method involving collagen content to improve the accuracy of assessing tumor response to NAC.

2. Methods and materials

2.1 Imaging system

Based on a previously demonstrated 9-wavelength hybrid FD and CW NIRST system [25], a new 12-wavelength system has been developed, as shown in Fig. 1. All laser sources, detectors, data acquisition modules, fiber bundles and computer are housed in a portable cart (Fig. 1(a)). As shown in Fig. 1 (b), Lights from six FD laser diodes (centered at wavelength of 661nm, 730nm, 785nm, 808nm, 830nm and 852nm), and six CW laser diodes (centered at wavelength of 850nm, 905nm, 915nm, 940nm, 975nm and 1064nm) are coupled together through two 6x1 fiber combiners, and then delivered to the tissue through sixteen custom 3-meter long bifurcated fiber bundles. The breast tissue is slightly compressed by an adjustable football-shaped fiber-breast interface that houses the ends of each of the sixteen fiber bundles. One of the other ends of these 16 fiber bundles is coupled to the output fiber of FD and CW sources, and the transmittance/reflectance light surrounding the breast tissue is collected by the other fifteen fiber bundles. The photomultiplier/photodiode detection module enables both FD and CW acquisitions.
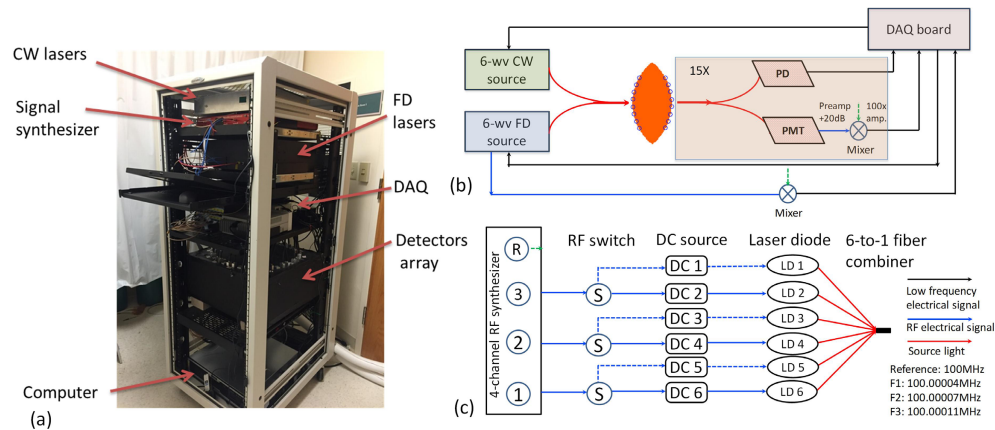

Fig. 1. The 12-wavelength FD-CW NIRST system. (a) A photo of the NIRST system. (b) The schematic for simultaneous FD and CW acquisition. (c) The system diagram for the 6-wavelength FD source module.

Figure 1(c) shows the system diagram of the recently developed 6-wavelength FD source module. The data flow of low frequency (~100Hz) electrical signal, radio frequency (~100 MHz) electrical signal and light are represented by black, blue and red solid lines, respectively. A multi-channel synthesizer (HS2004, Holzworth Instruments, USA) provides three RF channels of signals with the same power of 13dB but at slightly different frequencies of F1 = 100.0004MHz, F2 = 100.0007MHz, and F3 = 100.0011MHz, respectively. The 4th channel of the synthesizer provides a reference at the frequency of 100MHz for mixing and low frequency lock-in detection. The outputs of the first three RF signals are connected each to two RF inputs of FD laser diodes by three single-pole-double-throw (SPDT) RF switches, and combined with each of six DC current inputs through six bias-T couplers, to drive six FD

laser diodes. A customized six-to-one fiber combiner (Optical Fiber Systems Inc, NH) combined the light from six laser diodes into a single source fiber for the FD source output. The six FD diodes were divided evenly into two sets, with one represented by solid blue lines (661, 730nm and 785nm) and the other one by dashed lines (808nm, 830nm and 852nm). At one time, only three laser diodes (661nm/808nm, 730nm/830nm, and 785nm/852nm) are turned on and modulated by RF signals through the SPDT RF switches. Similarly, the six CW laser diodes are also divided into two sets of three lasers diodes (850nm/1064nm, 915nm/940n and 905nm/975nm) and each set is modulated by low frequency sinusoidal signals (50Hz, 90Hz, 110Hz) generated directly from the data acquisition board (USB 6255, National Instruments). Two sets of simultaneous acquisition were completed, involving three FD wavelengths and three CW wavelengths each, contributing to a complete measurement that included 12 wavelengths, covering a wavelength range from 661nm to 1064nm. The total power of any six FD + CW sources used at one time is less than 150mW, and the cross-talk between different channels was found to be less than 1%.

A custom programmable mechanical rotary switch consisting of one pair of the output branch fiber of the source couplers and 15 pairs of PMT (H9305-3, Hamamatsu, Japan) and silicon photodiode detectors (PD, C10439-03, Hamamatsu, Japan) was used to achieve 240 pairs of source-detection path-lengths. Two layers of long pass filters (850nm) were used to cover the front of each of PDs to eliminate short wavelength FD light. The RF output from the PMT detectors was amplified and filtered by a 20dB low-noise preamplifier, and then heterodyned down to the low frequencies of 400Hz, 700Hz and 1100Hz with mixing to a 100MHz reference signal through the RF mixers. These low frequency signals were then amplified (100X), filtered and read by a DAQ board (USB 6255, National Instruments). A digital lock-in detection technology was used to separate the mixed electronic signals (read by DAQ board) into three channels corresponding to the diffused light at each of three FD wavelengths, and obtain the amplitude and phase data of each channel respectively. For CW signal detection, the output of each PD detector was directly connected to the DAQ board. With digital Lock-in detection at three modulating frequencies, only the amplitude of the detected CW light signal was extracted at each of the three CW channels.

For each set of three FD and three CW wavelengths, the rotary switch was incremented 15 times to delivery source light into breast tissue from different fiber positions, and a similar data acquisition process was repeated 15 times, leading to a total of $16 \times 15 = 240$ measurements. The full data acquisition was completed by sequentially acquiring two sets of data at 12 wavelengths.
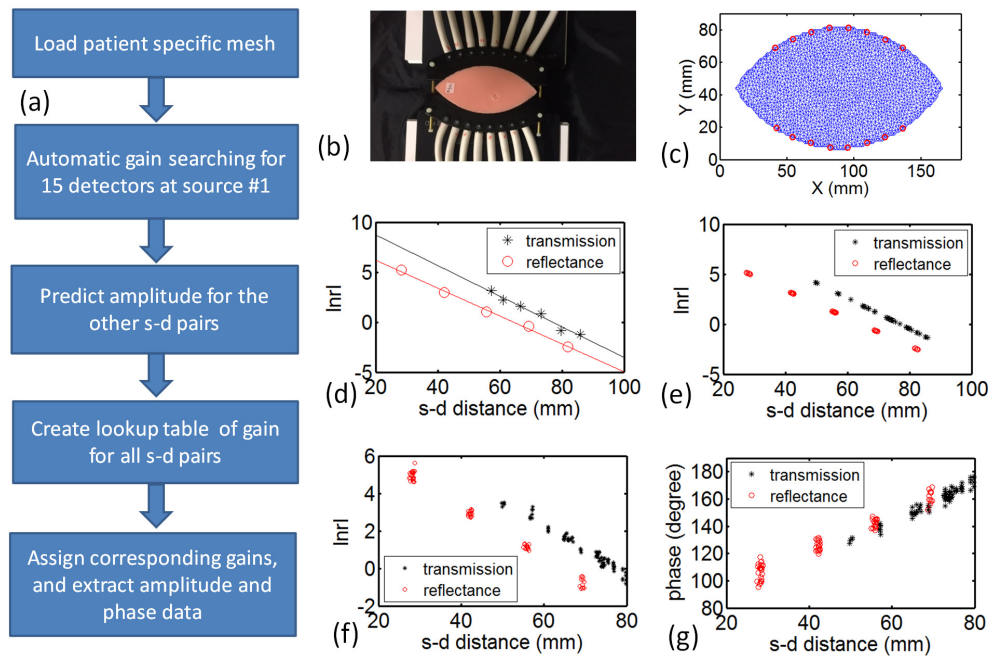
2.2 Prospective gain setting method

Fig. 2. Prospective gain adjustment of PMT detectors. (a) Flow chart illustrating the prospective gain adjustment scheme. (b) A photo of the adjustable fiber-breast interface (c) Corresponding football shape mesh created with 16 fibers assigned along the surface. (d) Amplitude data acquired at source position #1 using automatic point-by-point gain adjustment scheme. (e) Amplitude predicted for the other source-detector pairs, based on the parameters fitted from (d). (f) The actual amplitude and (g) phase data acquired using the gain from the lookup table for the rest of source-detector pairs.

Figure 2(a) outlines the chart illustrating the prospective gain adjustment scheme. First, the separation between two half-moon fiber plates was measured before breast/phantom experiments (Fig. 2(b)), and loaded into the data acquisition program, and then a patient/phantom specific mesh was generated automatically (Fig. 2(c)). An automatic point-by-point gain searching algorithm was applied to search and set the gain for each PMT when light source was delivered to position #1. In this point-by-point gain search algorithm, the gain control voltage (adjustable 0 – 1.1V) of 15 PMTs was increased from 0.4V (with in increments of 0.1V) until the AC component of the amplified output signal reached at least 0.1V, or the highest possible gain setting was reached. The acquired amplitude times source-detector distance in log scale is plotted versus source-detector distance for 15 PMT detectors. Using diffusion theory estimation on the given finite element mesh, a linear regression was applied to transmittance (black) and reflectance (red) data, shown in Fig. 2(d), to extract regression coefficients. The source-detector distance was calculated at each source-detector pairs, as seen in Fig. 2(e). The amplitude at each source-detector pair could then be predicted and the optimal PMT gain could be assigned from a premeasured lookup table of values for the optimal gain versus amplitude value.

2.3 Image reconstruction

An open source software platform, NIRFAST [26], was used to process and calibrate boundary amplitude and phase data, make patient specific 2D FEM meshes, and reconstruct optical NIRST images. 2D spatial images of absorption related chromophore concentrations of oxy and deoxy-hemoglobin, water, and lipid content, and scattering amplitude and

scattering power were reconstructed, using a reconstruction method with hybrid FD and CW data set [25]. The absorption spectrum of collagen content was encoded into the reconstruction procedure as well, which enabled tomographic recovery of collagen content, in addition to the other four chromophores. The absorption spectrum used in this study was referred to Taroni *et al* [23]. It was obtained from measurement of collagen type 1 powder from bovine Achilles tendon. A fixed regularization parameter of 1 have been used in this paper for both simulation and human subject studies, together with a stopping criterion of 10 iterations or when the projection error was less than 2% of previous iteration value.

2.4 Numerical simulation

Numerical simulations were performed to evaluate the effect of presence of collagen in the image reconstruction process. The mesh was generated as shown in Fig. 2(c), consisting of 2118 nodes that correspond to 3858 triangular elements. 16 co-located source-detector (fiber) positions were placed along two sides of the mesh, shown by red circles. Each group of eight fibers was placed along an arc with radius of 101mm, and two adjacent fibers have an angular separation of 4.65 degrees. Given optical properties/chromophore concentrations assigned for each node, the simulated data set was generated with 1% noise added in amplitude and phase data at each wavelength. Optical images were reconstructed using a reconstruction pixel basis of 30×30, and the algorithm was iterated until the stopping criterion was reached [27].

For image analysis, the region of interest (ROI) was segmented from reconstructed HbT images, with the full-width-at-half-maximum (FWHM) criterion. The inclusion/background contrast was defined as the average value in the segmented ROI to that in the background.

2.5 Phantom experiment

Phantom experiments were conducted to compare the performance of different gain adjustment methods. A mold was designed and fabricated through 3D printing, in order to make gelatin phantoms with cross-sections matching the desired shape of breast under the breast-fiber interface. Phosphate Buffered Saline (PBS), type 1 Agarose (A6013 SIGMA-ALDRICH), 1% Intralipid (20% I.V. Fat Emulsion, Fresenius Kabi), and whole porcine blood were used to provide optical properties similar to normal breast tissue.

2.6 Subject imaging

All human subject imaging was carried out under a protocol approved by the Committee for the Protection of Human Subjects (CPHS) at Dartmouth-Hitchcock Medical Center. Written consent was obtained for each subject and the study procedure was fully explained. During the imaging session, subject was sitting in a recline chair with fiber-breast interface placed at the desired plane/orientation to maximize tumor coverage. A dark blue sheet was covered on the patient to minimize the ambient light interference in the light signals. Nine normal subjects and one breast cancer patient (invasive ductal carcinoma (IDC)) were imaged. The normal subjects and patient data were reconstructed with and without collagen included.
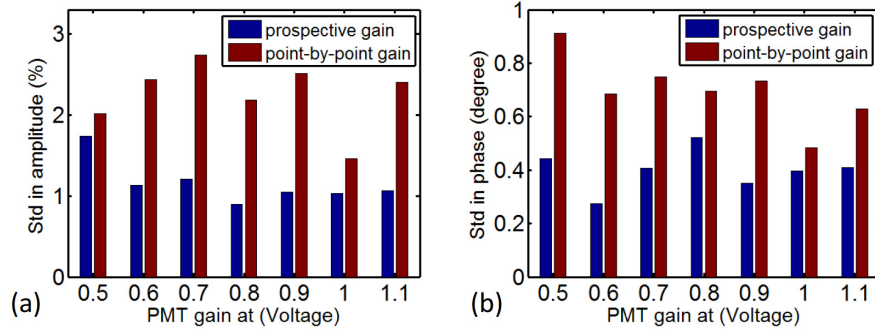
3. Results

Fig. 3. Standard deviation in amplitude (a) and phase (b) of 30 consecutive measurements using prospective and point-by-point gain setting schemes.

Figure 3 shows the signal variation (standard deviation) in amplitude (a) and phase (b) of 30 consecutive measurements, using previous prospective (red) and point-by-point (blue) gain setting schemes, respectively. It is clearly seen that the prospective acquisition scheme has superior performance to the previous one, in terms of signal stability for both amplitude and phase, at all PMT gains from 0.5 to 1.1. The FD data acquired using the prospective gain adjustment scheme has an average standard deviation of 1.1% and 0.3 degree in amplitude and phase, respectively, compared with 2.1% and 0.7 degree using the previous gain adjustment method. In addition, the prospective gain setting scheme reduced the data acquisition time including all 240 source-detector pairs to 55 seconds, from 90 seconds with prospective gain setting scheme that searches for optimal gain at each of 240 source-detector pairs.
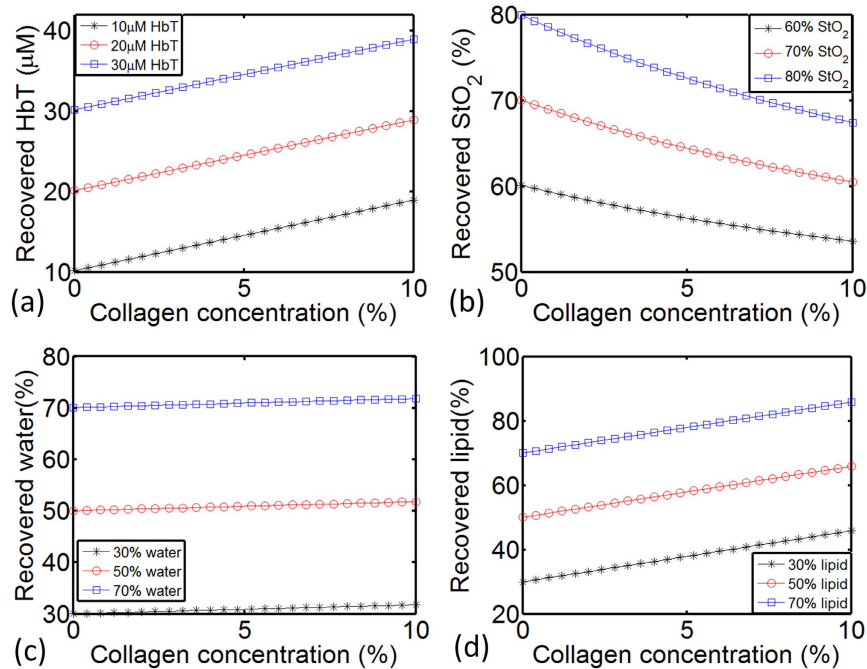

Fig. 4. Recovered HbT (a), StO$_2$ (b), water (c) and lipid (d) in a simulated homogeneous phantom, with collagen content increased from 0 to 10%.

Background collagen concentration with a range of 0 to 8.5% was reported in human subjects by Taroni *et al* in Reference [28]. A slightly higher value of 10% has been used in the simulation studies in this paper. Figure 4 shows the recovered chromophore concentration of four major absorbers in a simulated homogeneous phantom when background collagen content increased from 0 to 10%. HbT of 20uM, StO$_2$ of 70%, Water of 50%, Lipid of 50%, SA of 0.8 and SP of 0.3 were assigned for each node as the default background value. Varying concentration of collagen was added to generate the forward data. However, when the collagen was not included in the reconstruction, the absorption portion due to the collagen in the forward data will result in overestimated recovery in other chromophores. As shown in Fig. 4, when collagen content increased from 0% to 10%, overestimation in HbT, water and lipid, as well as underestimation in StO$_2$ can be observed from the recovered values. The overestimate increases linearly with the concentration of collagen added. With 10% collagen, there was an overestimate of 8.9uM, 1.8% and 15.8% in the recovered HbT, water and lipid, respectively. These overestimates stayed the same, regardless of the actual assigned HbT, water and lipid changed in the range of 10uM - 30uM, 30% - 70% and 30% - 70% respectively. Meanwhile, the underestimate in StO$_2$ decreased nonlinearly versus increasing collagen concentration. With 10% collagen, there was an underestimate of 12.6%, 9.5% and 6.5% in the recovered StO$_2$ for actual StO$_2$ assigned at 80%, 70% and 60%, respectively.
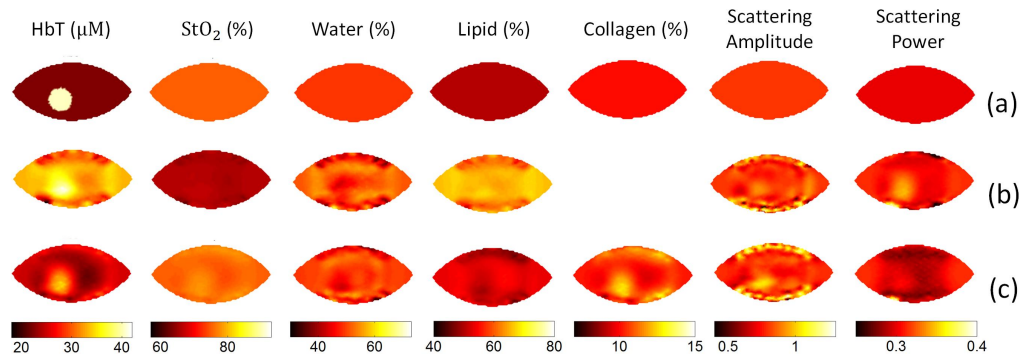

Fig. 5. Reconstructed images of a simulated heterogeneous phantom. (a) Images with true values, with a circular inclusion with diameter of 2cm. An inclusion/background contrast of 2 is assigned to HbT, with homogeneous background value of 75%, 50%, 50%, 10%, 0.8 and 0.3 assigned for StO2, water, lipids, collagen, SA and SP, respectively. Reconstructed images without collagen (b) and with collagen included (c).

Figure 5 showed the reconstructed images without collagen (Fig. 5(b)) and with collagen (Fig. 5(c)), using a simulated heterogeneous phantom. An inclusion/background contrast of 2 was assigned to HbT, with true values of 40uM and 20uM assigned in the inclusion and background, respectively. Homogeneous background values of 75%, 50%, 50%, 10%, 0.8 and 0.3 were assigned for StO$_2$, water, lipids, collagen, SA and SP, respectively. As shown in Fig. 5(b), the recovered HbT of 31.0uM in the background was significantly overestimated, resulting in an underestimated recovered contrast of 1.3. In contrast, with collagen included in the reconstruction, the recovered contrast of HbT increased to 1.6. Considering that the assigned collagen content was homogenous, the inclusion/background contrast in reconstructed collagen image of 1.2 indicates possible crosstalk between HbT and collagen.

The same procedure was repeated for StO$_2$, water, and lipid, respectively, in the presence of 10% of background collagen. When collagen content was not included in the reconstruction process, the recovered contrast of StO$_2$, water and lipid decreased by 8.3%, 4.5% and 14.3%, respectively, compared with the case where collagen was included in the reconstruction, given true contrast of 1.3, 1.5 and 1.5.
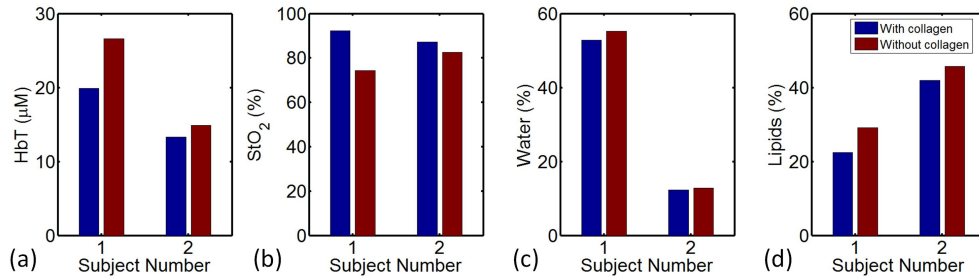
Fig. 6. Contents of breast tissue recovered for HbT (a), StO2 (b), Water (c) and Lipids (d), with and without collagen included in reconstruction. The radiographic density type of subject #1 and #2 is heterogeneously dense (HD) and scattered fibroglandular dense (Scattered), respectively.

Figure 6 shows the comparison of estimated chromophore concentrations of two normal subjects with and without collagen included in the reconstruction process. The radiographic density type of subject #1 and #2 is heterogeneously dense (HD) and scattered fibroglandular dense (Scattered), respectively. The recovered background collagen content of subject #1 and #2 is 4.8% and 1.3%, respectively. Compared with reconstruction without collagen included, reconstruction with collagen yields in 6.7uM & 1.6uM lower HbT, 17.8% & 4.7% higher StO$_2$, 2.8% & 0.5% lower water, and 6.7% & 3.8% lower lipids, for subject #1 & #2, respectively.

A total number of nine normal subjects were imaged, and similar comparison was performed for each subject. Tomographic images were reconstructed of collagen and the other four chromophores using spectral data set acquired from the FD-CW NIRST system. Average background collagen concentration was then calculated for each subject using the reconstructed collagen image. Average collagen content with a range of 0 to 4.8% was found in breast tissue among all the subjects, together with an increase in HbT from 0 to 6.7uM, 0 to 2.8% in water, and 0 to 6.7% in lipid, and decrease in StO2 from 0 to 17.8%, when collagen was included in the reconstruction.
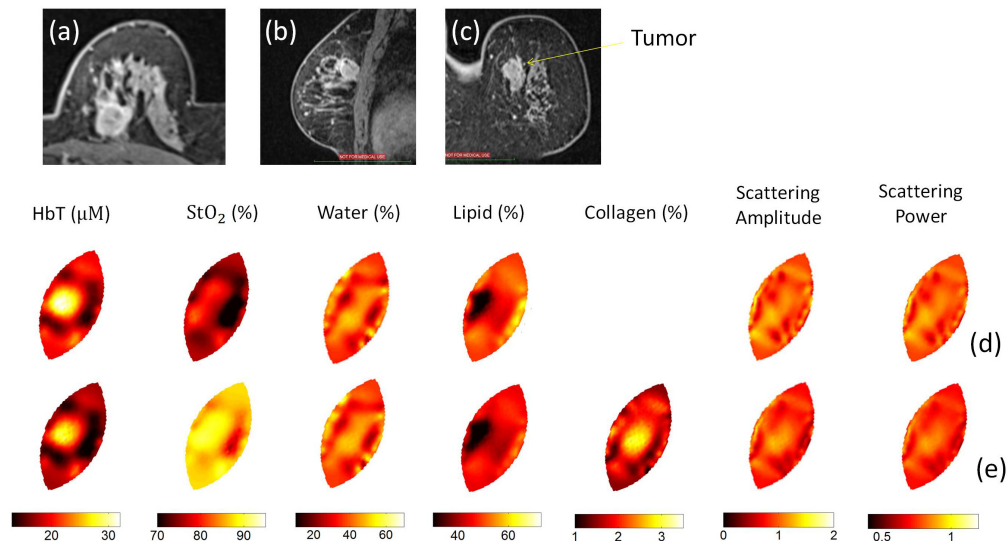

Fig. 7. MRI T2 images of a patient with invasive cancer in the left breast: (a) Axial view, (b) sagittal view and (c) coronal view. Reconstructed optical images without (d) and with (e) collagen included. Recovered optical images are displayed in the same orientation in (d) and (e) as in (c).

Figure 7 shows the MRI and reconstructed optical images of a breast cancer patient imaged with the NIRST system. This 63-year old woman has a 2 cm invasive ductal carcinoma (IDC) tumor in her left breast. The position of the tumor was marked in advance on the breast surface according to her prior MRI to guide placement of the fiber-breast interface during optical imaging. The optical images were reconstructed without (Fig. 7(d)) and with (Fig. 7(e)) collagen included. Orientation of the breast mesh (2-8 o'clock) was adjusted to coincide with the coordinate system in MRI, as shown in Fig. 7(d)-7(e). The recovered inclusion/background contrast in HbT increased from 1.5 to 1.7 when collagen was included in the reconstruction. A contrast of 1.2 was found in the recovered collagen image, with an average background collagen concentration of 2.3%.

4. Discussion

This system demonstrated here, was able to acquire data at 12 wavelengths, and has been developed and validated for breast cancer patient imaging. Two sets of simultaneous acquisitions involving three FD wavelengths and three CW wavelengths cover a total of 12 wavelengths with a range from 661nm to 1064nm. More FD wavelengths were added to increase the spectral resolution in the short wavelength range, on which the reconstruction of oxy- and deoxy-hemoglobin depends most. Meanwhile, a better estimate of scattering properties can be expected with more FD wavelengths using approximations to Mie theory which constrain the spectrum to a power function. In the past, this type of scatter spectrum constraint was found to be critical for better quantification of the absorption coefficients at longer CW wavelengths, and thus more accurate reconstruction of water and lipid might be achieved with this addition [24].

Frequency domain measurements using intensity-modulated sources are stable and cost effective [29], and PMT detectors are widely used in most FD near infrared spectral tomography systems. With external DC voltage from 0V to 1.1V applied as the gain of PMT detectors, a wide range of linear responses could be achieved. Depending on the specific FD NIRST system and light sampling geometry, PMT detectors at different positions, relative to the source, receive levels of light which could be different by orders of magnitude. In order to account for the dynamic variability, various voltage gains need to be assigned for each of 15 individual PMT detectors. Two gain setting schemes were used in our previous studies [30, 31]. The fixed gain scheme has been traditionally used for circular geometry, where source-detector distance does not change for a given PMT detector during the acquisition regardless of the position of source fiber. An automatic point-by-point PMT setting approach was developed by El-Ghussein to accommodate an irregular fiber-breast interface [30]. In this approach, the corresponding gain is automatically found and applied at each of 240 source-detector pairs (point-by-point) to ensure the detected light intensity in the optimal linear response range. Though the latter approach worked for more complicated geometries, it suffered from longer acquisition times and larger signal variations because of the rapid changes in gain and the longer settling times of PMTs. In addition, unexpected patient movement during the longer 90 second measurements may have contributed to errors from motion artifacts. In order to accelerate the data acquisition and thus reduce motion artifacts, the new gain setting scheme was developed, shown in Fig. 2. It took advantage of the fast acquisition speed of a fixed gain setting method, and the flexibility of the dynamic point-by-point gain setting method. The optimal gain values were automatically found using a single spot gain setting method at source position #1, and the prospective gains for other locations were estimated from a lookup table that was applied to the subsequent source-detector pairs when the source was delivered from the other 15 positions. With this prospective gain setting method, the acquisition time was reduced by almost 40% to 55s, from 90s with the previous dynamic point-by-point gain setting method. In addition, better stability was achieved in both amplitude (Fig. 3(a)) and phase (Fig. 3(b)) data with the new gain adjustment method.

Limited by the lack of data at wavelengths longer than 850nm, most near infrared imaging/spectroscopy systems target on the quantification of up to four major absorbers of oxy- and deoxy-hemoglobin, water and lipid, ignoring the other chromophores in breast. This all comes about because most higher gain PMTs suffer from photocathodes that have poor performance above this wavelength range, which may result in overestimation/underestimation in the above four major absorbers. Collagen is another important chromophore in breast tissue. Taroni and associates did an extensive set of studies on collagen quantification in human breast, who first measured collagen absorption spectrum, quantified collagen in vivo [28] and showed collagen images [32]. Using this recently developed 12-wavelength system, incorporating more CW wavelengths, it was possible to extract tomographic images of collagen content in breast tissue. Both simulation and patient imaging were performed in order to quantify collagen in breast tissue and investigate the effect of presence of collagen on the reconstruction of other chromophores.

The absorption due to collagen content would contribute to the recovery of other chromophores, and results in an overestimation in all other four chromophores, when collagen was not included in the reconstruction procedure, as shown in Fig. 4. Depending on the absorption spectrum of each chromophore and the wavelengths utilized to generate forward data, the amount of overestimate varied between chromophores. As shown in Fig. 4(b), deoxy-hemoglobin is more sensitive to the presence of collagen than oxy-hemoglobin, which leads to the underestimate in oxygen saturation. In addition, with the same amount of added collagen content, recovered StO_2 suffers more underestimate in the case of higher StO_2. Comparing Fig. 4(c) and Fig. 4(d), it was found that given the same amount of 10% collagen added into the background, the overestimate in water (1.8%) is much less than that in lipid (15.8%). This may be because one absorption peak of lipid (at 926nm) is very close to one peak of collagen (at 913nm) and the ignored absorption from collagen was accounted in lipid.

Insufficient recovery of tumor to normal-surrounding-tissue contrast is always a challenge in diffuse tomographical image reconstruction. In addition to the diffusive nature of photon transport in biological tissue, the existence of chromophores other than four major absorbers may also make a contribution. The simulation results presented in Fig. 5 clearly show suppression in recovered contrast in HbT due to the presence of collagen, when collagen was ignored during the reconstruction process. With 10% of collagen added in the background, the recovered HbT contrast increased by 23.1% when collagen was included in the reconstruction, as compared to the case where collagen content was ignored in the reconstruction procedure.

Nine normal subjects and one cancer patient were imaged with the new 12-wavelength NIRST system. Comparing the reconstructions with and without collagen, there was lower HbT, water and lipid, and higher StO_2 observed when collagen was included into the reconstruction estimation process. This result is consistent with the simulation results, and the patient data reported by Taroni *et al* [13, 28]. However, the change in lipid between with and without collagen in the image reconstruction in this study is significantly higher than that reported by Taroni. This may be explained by the fact that different wavelengths have been used to extract chromophore contents in our NIRST system, and there are major differences in the nature of the signal acquisition (time domain system vs FD + CW system here), as well as large potential differences in the fitting algorithms. As shown in Fig. 7, the recovered contrast in HbT increased from 1.5 to 1.7 when collagen was included in the reconstruction. HbT contrast has been always presented as the most important indicator in breast cancer diagnosis and tumor response monitoring to neoadjuvant chemotherapy (NAC). A more accurate quantification of the HbT contrast is important to provide better separation between malignant and benign lesions, and this can also provide more robust prediction of tumor response to NAC at the early stages. Additionally, the recovered contrast of 1.2 in collagen content was observed in a case study, and further patient studies are expected to validate whether collagen contrast can be a new biomarker for breast cancer detection.

5. Conclusion

A portable 12-wavelength frequency-domain (FD) and continuous-wave (CW) near infrared spectral tomography (NIRST) system has been developed for breast cancer detection and NAC treatment monitoring. A novel prospective gain setting scheme of PMT detectors was developed to significantly expedite data acquisition and to reduce signal variation. Besides oxy- and deoxy-hemoglobin, water and lipid, image reconstruction with and without collagen was conducted in both simulation and human subject experiments. When collagen was not included into the reconstruction, overestimate in recovered HbT, water and lipid, as well as underestimate in StO_2, have been observed. Both simulation and patient studies showed that the recovered inclusion/background contrast in HbT increased when collagen was included into the reconstruction, in the presence of background collagen.

Disclosures

The authors declare that there are no conflicts of interest related to this article.